Dynamics of excitons in individual InAs quantum dots revealed in four-wave mixing spectroscopy

Q. Mermillod,[1,2,*] D. Wigger,[3,†] V. Delmonte,[1,2] D. E. Reiter,[3,‡] C. Schneider,[4] M. Kamp,[4] S. Höfling,[4,5] W. Langbein,[6] T. Kuhn,[3] G. Nogues,[1,2] and J. Kasprzak[1,2,§]

[1] *Univ. Grenoble Alpes, F-38000 Grenoble, France*
[2] *CNRS, Institut Néel, "Nanophysique et semiconducteurs" group, F-38000 Grenoble, France*
[3] *Institut für Festkörpertheorie, Universität Münster, 48149 Münster, Germany*
[4] *Technische Physik and Wilhelm Conrad Röntgen Research Center for Complex Material Systems, Universität Würzburg, Germany*
[5] *SUPA, School of Physics and Astronomy, University of St Andrews, St Andrews, KY16 9SS, United Kingdom*
[6] *Cardiff University School of Physics and Astronomy, The Parade, Cardiff CF24 3AA, United Kingdom*

A detailed understanding of the population and coherence dynamics in optically driven individual emitters in solids and their signatures in ultrafast nonlinear-optical signals is of prime importance for their applications in future quantum and optical technologies. In a combined experimental and theoretical study on exciton complexes in single semiconductor quantum dots we reveal a detailed picture of the dynamics employing three-beam polarization-resolved four-wave mixing (FWM) micro-spectroscopy. The oscillatory dynamics of the FWM signals in the exciton-biexciton system is governed by the fine-structure splitting and the biexciton binding energy in an excellent quantitative agreement between measurement and analytical description. The analysis of the excitation conditions exhibits a dependence of the dynamics on the specific choice of polarization configuration, pulse areas and temporal ordering of driving fields. The interplay between the transitions in the four-level exciton system leads to rich evolution of coherence and population. Using two-dimensional FWM spectroscopy we elucidate the exciton-biexciton coupling and identify neutral and charged exciton complexes in a single quantum dot. Our investigations thus clearly reveal that FWM spectroscopy is a powerful tool to characterize spectral and dynamical properties of single quantum structures.

I. INTRODUCTION

A comprehensive understanding of exciton complexes and their transitions in semiconductor quantum dots (QDs) is a crucial step for assessing their functionality as optically controllable solid state devices in quantum information technology [1–3]. For example, for ultrafast manipulation of QDs it is essential to know the decay and decoherence times of exciton and biexciton [4–6], while for entangled photon generation, the fine structure splitting (FSS) between the excitons and the biexciton binding energy (BBE) play a decisive role [7–11]. Also the alignment between the polarization of the light and the QD axis becomes important when selectively addressing different transitions [12]. In our study we can access all these quantities, i.e., dephasing and lifetimes, FSS, BBE and dot axis of a single QD, within the same set-up. For the experimental investigations we implement a heterodyne spectral interferometry technique [13] to retrieve polarization-resolved four-wave mixing (FWM) signals. While FWM has often been used to infer exciton dynamics in QWs [14] or for QD ensembles [15], for single QDs the experiments are more challenging because of the weak signal intensity. This long-standing issue has recently been solved by exploiting photonic nanostructures to enhance non-linear responses. Employing low-Q planar microcavities [16], conical photonic waveguide antennas [17] and deterministic micro-lenses [18] the detection sensitivity of FWM generated by an exciton is improved by up to four orders of magnitude with respect to QDs in bulk material. To model the data we use a density matrix formalism including all populations and coherences, as well as decay and decoherence rates [19, 20]. In this paper we present a comprehensive set of measurements and simulations, exploring the oscillatory dynamics of coherences and populations in the exciton-biexciton system in a single QD.

Because the QDs in our sample exhibit charge fluctuation, we can also study coherent dynamics of more involved complexes, namely charged excitons. To discriminate between neutral and charged excitons we use two-dimensional (2D) FWM spectroscopy. In 2D FWM spectra transitions correspond to peaks on the diagonal, while the coupling between different states can be seen by off-diagonal peaks connecting the diagonal ones [21–23]. We show that this technique allows for a fast, comprehensive characterization of exciton complexes.

The paper is organized as follows: First, we focus on the exciton-biexciton system introducing the states, their energies and couplings. After characterizing quantum beats induced by the FSS and the BBE, we analyze the angle dependence of the dynamics. In a next step, we look at the population dynamics revealing coherences that are typically hidden. Finally, we study 2D FWM

* quentin.mermillod@neel.cnrs.fr
† d.wigger@wwu.de
‡ doris.reiter@wwu.de
§ jacek.kasprzak@neel.cnrs.fr

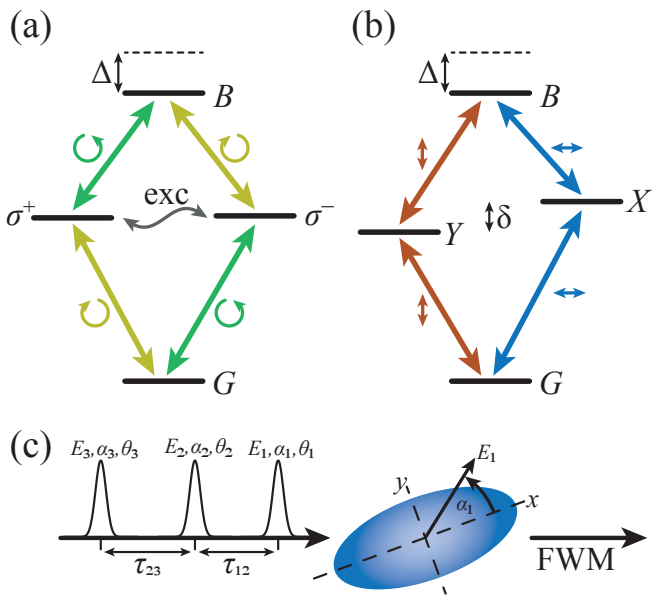

FIG. 1. **Schematic picture.** Sketches of the QD system for (**a**) circularly polarized excitation and (**b**) linearly polarized excitation. (**c**) Cartoon of the FWM experiment and the QD orientation.

maps identifying neutral and charged exciton complexes.

II. EXCITON-BIEXCITON SYSTEM

A. QD system and FWM

In this work, we perform FWM measurements of strongly-confined excitons in individual InAs QDs, embedded in a low-Q asymmetric GaAs/AlGaAs microcavity. A detailed description of the sample growth and characterization can be found in the Methods section. In the first part we restrict ourselves to the neutral s-shell excitons in the QD. Depending on the polarization of the exciting pulses, excitons with different polarizations are created. For circular polarization denoted by ↻ and ↺, the system is characterized by the ground state $|G\rangle$, the two exciton states $|\sigma^+\rangle$ and $|\sigma^-\rangle$ and the biexciton state $|B\rangle$ as depicted in Fig. 1 a. The energy of the biexciton state is reduced with respect to the double exciton energy by the BBE, denoted as Δ. The degeneracy of the two excitons is lifted by the anisotropic confinement potential of the QD and its zinc-blende crystal structure leading to an exchange coupling between the excitons. Therefore, the circularly polarized states are not the energy eigenstates of the system. Instead, the eigenstates are given by the linearly polarized excitons $|X\rangle = (|\sigma^+\rangle + |\sigma^-\rangle)/\sqrt{2}$ and $|Y\rangle = i\,(|\sigma^+\rangle - |\sigma^-\rangle)/\sqrt{2}$, which are split by the FSS, labeled as δ (see Fig. 1 b). We define the polarization axis of the X-exciton as the x-axis of the QD and specify the angle of a linearly polarized excitation with respect to this axis, i.e., for $\alpha = 0°$ the X-exciton is excited, while for $\alpha = 90°$, the Y-exciton is generated as depicted in Fig. 1 c. In these particular cases, the four-level system of the QD can be restricted to three-levels. For any intermediate angle α a linear combination of X- and Y-exciton is created. We will indicate the light polarization angles $\alpha = (0°, 45°, 90°, 135°)$ by $(-, \diagup, |, \diagdown)$.

In practice, three laser pulses E_i $(i = 1, 2, 3)$ with pulse areas θ_i and polarization angles α_i drive FWM of the QD, as depicted in Fig. 1 c. The optical frequencies of E_i are shifted by Ω_i using acousto-optic modulation in the radio-frequency range. The polarizations of the beams are adjusted by a set of $\lambda/2$ and $\lambda/4$ plates. The delays between the pulses are denoted by τ_{12} and τ_{23}, which are handled by a pair of mechanical delay stages. A positive delay corresponds to the case when the first pulse arrives before the second and so on. The beams are then recombined into the same spatial mode and focused onto the top of the sample placed in a cryostat operating at $T = 5$ K using an external microscope objective optimized for NIR spectral range (NA= 0.65), installed on a XYZ-piezo stage. The investigated nonlinear polarization is retrieved by detecting the corresponding phase modulation in reflectance using a heterodyne technique with a reference beam E_r. Our detection scheme combines optical heterodyning with spectral interferometry, as detailed in Ref. [24]. The current implementation is presented in Ref. [16].

With FWM, we can probe population and coherence dynamics of a QD exciton. To detect the latter, the time delay τ_{23} between E_2 and E_3 is set to zero, i.e., we only use E_1 and E_2 and heterodyne at $2\Omega_2 - \Omega_1$: the first arriving pulse creates a coherence in the system, which after τ_{12} is transformed into FWM signals by the second pulse. The ratio of their pulse areas is taken to be $\theta_2 = 2\theta_1$. To explore the population dynamics, an excitation with three beams is required and we look at the heterodyne signal at $(\Omega_3 + \Omega_2 - \Omega_1)$. All pulses have the same area $\theta_i = \theta$. The first laser pulse creates the coherence. The second one, which follows shortly after at $\tau_{12} = 0.5$ ps (yet beyond the overlap of E_1 and E_2 to avoid the generation of non-resonant nonlinearities), creates populations evolving during τ_{23}. The FWM signals are then launched by the third pulse, E_3.

In the calculations the density matrix elements are denoted by $\varrho_{\nu\nu'}$ with $\nu \in \{G, \sigma^+, \sigma^-, B\}$ in the circularly polarized basis and $\nu \in \{G, X, Y, B\}$ in the linearly polarized basis. The equations of motion under an excitation with a series of ultrafast pulses are solved analytically following Refs. [19] and [20]. In between the pulses, the coherences and populations are subject to decay and decoherence, where the following rates are taken into account: The decay of the populations is included by the rate $\gamma = 1/T_1$ for all transitions between biexciton and exciton, as well as between exciton and ground state, where T_1 is the radiative lifetime. The corresponding coherences ϱ_{GX}, ϱ_{GY}, ϱ_{XB} and ϱ_{YB} have a decoherence rate of $\beta = 1/T_2$, which includes the dephasing

caused by the finite lifetime. Note that T_2 is typically called dephasing time. The coherence between ground and biexciton state ϱ_{GB} decays with the rate β_B and the coherence between the single exciton states ϱ_{XY} is subject to decoherence with the rate β_{XY}. Details on the Hamiltonian and the equations of motion can be found in the Methods section. To compare experimental data and theoretical predictions, we fitted the analytical formulas to the data using independently determined FSS δ, the biexciton binding energy Δ and the decay and dephasing rates as fitting parameters. The retrieved decay and decoherence times correspond to the values used for the theoretical curves.

A crucial input into further results are pulse areas θ_i. When varying the latter, the QD exciton undergoes Rabi rotations [25, 26]. In the two-level system a pulse area of π is attained when a complete transition from the ground state to the exciton state takes place. In FWM, where the coherence is probed, the signal is expected to follow a $|\sin(\theta_1)|$ dependence, where the first maximum is at $\pi/2$ when the polarization is maximal. Thus, it is a prerequisite to determine the relation between the measured driving intensities $P_i = E_i^2$, to their pulse areas $\theta_i = \int \mu |E_i(t)| \mathrm{d}t \sim \sqrt{P_i}$. To restrict ourselves to a two-level system we use circularly polarized light to excite and probe the system. In Fig. 2 b, we plot the FWM amplitude of the GX transition against $\sqrt{P_1}$, while the pulse intensity of the second pulse is fixed at $P_2 = 1$ µW. The maximum lies at $P_1 = 0.25$ µW (corresponding to approximately 10^3 photons per pulse E_1), which we identify as $\theta_1 = \pi/2$ pulse.

B. Classification of Quantum beats

The FSS δ and the BBE Δ both give rise to quantum beats, which are visible in different FWM signals as presented in Fig. 2. In the spectrum the energies δ and Δ can be determined as the difference between the respective spectral lines. Figure 2 a shows a single QD spectrum obtained from co-linearly $(-,-)$ polarized excitation. GX and XB line are clearly separated by $\Delta \approx 3$ meV. The inset shows a FWM spectrum obtained from co-circularly $(\circlearrowleft,\circlearrowleft)$ polarized excitation, where we can see the FSS between the two single excitons with $\delta \approx 38$ µeV.

In the time domain, the period of the beatings is related to the energy via $T_\delta = 2\pi\hbar/\delta$ and $T_\Delta = 2\pi\hbar/\Delta$. The FSS-induced quantum beat can best be seen for co-circularly polarized excitation, where no biexciton is excited as presented in Fig. 2 c. The laser pulses excite the $G\sigma$ transition, which is a linear combination of X and Y. When evolving in time, the $G\sigma$-coherence oscillates with the FSS. Indeed, the FWM amplitude which is a measure for the $G\sigma$-coherence as function of the delay τ_{12} displays pronounced quantum beats and an exponential decay [27–30], as reproduced by the theoretical calculations. The corresponding equation for the FWM signal

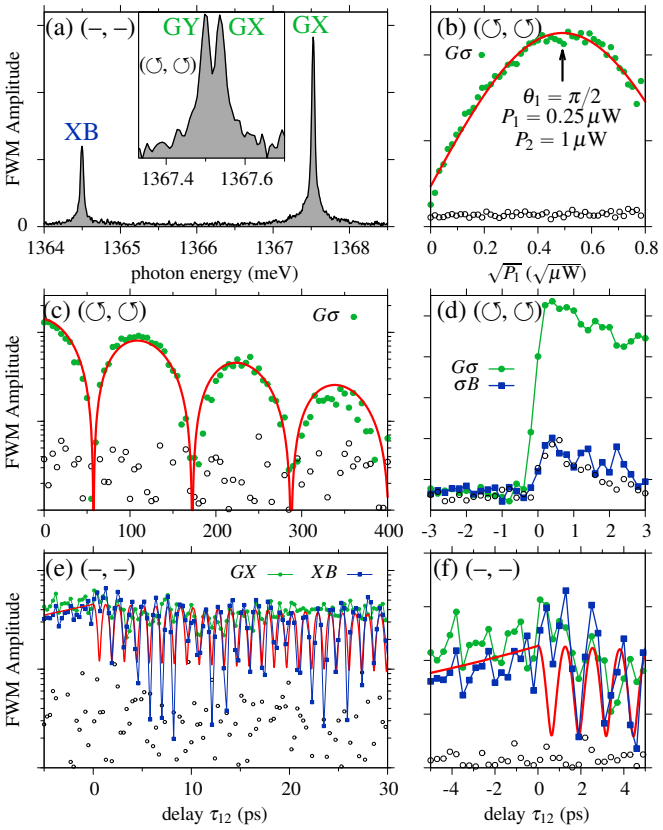

FIG. 2. **Quantum beats.** (**a**) Two-pulse FWM spectra of a single QD for co-linear polarization. Inset: Zoom in on the exciton line for co-circular polarization. (**b**) FWM signal as function of excitation intensity $\sqrt{P_1}$. (**c**) FWM signal as function of time delay τ_{12} for co-circularly polarized excitation. (**d**) Zoom-in of (**c**) around $\tau_{12} = 0$. (**e**) and (**f**) FWM signal as function of τ_{12} for linear polarization with $\alpha = 0°$. Green dots and blue squares: experimental data; gray circles: indication of noise level; red lines: theoretical calculation.

$\mathcal{S}_{\nu\nu'}$ is given by

$$\mathcal{S}_{G\sigma} \propto \exp\left(-\frac{\tau_{12}}{T_2}\right)\sqrt{\cos\left(\frac{\delta}{\hbar}\tau_{12}\right)+1}. \qquad (1)$$

The pulse area only determines the strength of the signal. Note, that for a pulse area being a multiple of π, no coherence $\varrho_{G\sigma}$ is excited and the FWM amplitude is zero. From Fig. 2 c we extract the period of the FSS-induced beating to $T_\delta = 115$ ps, which corresponds to $\delta = 36$ µeV in good agreement with the spectral measurement in Fig. 2 a. We retrieve a dephasing time of $T_2 = 200$ ps. Under circularly polarized excitation the FWM signal of the σB transition is suppressed (cf. Fig. 1 a) and accordingly there is no signal at the σB transition. When we zoom into the coherence dynamics at delays close to $\tau_{12} = 0$ in Fig. 2 d, we confirm that the σB transition does not exceed the background level, which for $\tau_{12} > 0$ is enhanced by the broadband emission of acoustic phonons generated by $G\sigma$. For negative time delays the FWM sig-

nal is zero since there is no two-photon coherence under circularly polarized excitation [30].

To determine the BBE Δ in the time domain, we excite with co-linear polarization along the QD axis, such that the system can be reduced to the three levels GXB (cf. Fig. 1 b). In this case, there is no FSS-induced quantum beat between the excitons, because we drive the energy eigenstate X, while the transitions GY and YB are not excited. This gives us the opportunity to solely study the BBE-induced quantum beat. The dynamics of the FWM signal is presented in Fig. 2 e, where the FWM signals of the GX and the XB transition are shown as function of the time delay τ_{12}. A strong oscillation of the XB signal with a period of $T_\Delta = 1.27$ ps is found, corresponding to a BBE of $\Delta = 3.25$ meV. These values are in good agreement with the spectral measurements in Fig. 1 a. The oscillation is also seen in the GX signal, but with a much weaker amplitude. The oscillation gets more pronounced with increasing pulse area. The dynamics can be described analytically with our formalism [31]. The general formula for arbitrary pulse areas is rather lengthy, therefore we give the equations which have been evaluated for our parameters, namely the polarization angle $\alpha = 0°$ and pulse area. With $\theta_1 = 3\pi/5$ we obtain

$$\mathcal{S}_{GX} \propto \exp\left(-\frac{\tau_{12}}{T_2}\right)\sqrt{4.36 + \cos\left(\frac{\Delta}{\hbar}\tau_{12}\right)}, \quad (2a)$$

$$\mathcal{S}_{XB} \propto \exp\left(-\frac{\tau_{12}}{T_2}\right)\sqrt{1.15 + \cos\left(\frac{\Delta}{\hbar}\tau_{12}\right)}. \quad (2b)$$

Note that the sign in front of the cosine is negative for pulse areas $\theta_1 < \pi/2$ and positive for pulse areas $\theta_1 > \pi/2$. For clarity we only show Eq. (2b) in Fig. 2 e and f.

For negative time delays a two-photon coherence ϱ_{GB} between ground state and biexciton is generated by the pulse E_2, which arrives first at the QD. Due to the reversed ordering this coherence is then transferred into the FWM signal by E_1 showing a decay in both GX and XB transition according to

$$\mathcal{S}^{\tau<0}_{GX,XB} \propto e^{-\beta_B \tau_{12}}. \quad (3)$$

This is in agreement with the signals shown in Fig. 2 e and f, where a fast decay for increasing negative time delays is observed.

Because the BBE-induced oscillation is much faster than the FSS-induced beating, to resolve them a much longer measurement time is required. Thus, in the following, we performed measurements such that the BBE oscillation is not resolved. We further note that the results in the following Secs. II C and II D were obtained from different QDs, which exhibit the same behavior but with different time constants.

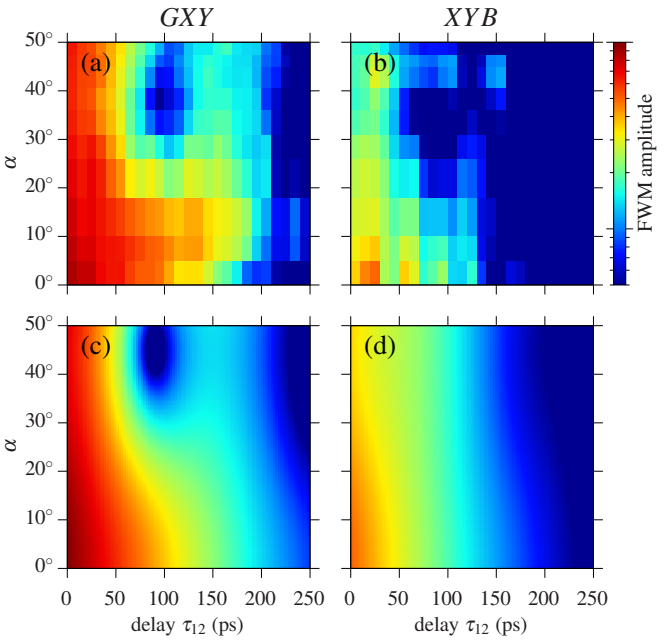

FIG. 3. **Coherence dynamics for co-linear excitation.** (**a,b**) Measurements and (**c,d**) calculations of the coherence dynamics as function of delay τ_{12} and polarization angle α for co-linear excitation for (**a,c**) the GXY transition and (**b,d**) the XYB transition.

C. Polarisation angle dependent coherence dynamics

As soon as the polarization of the exciting light field deviates from the strictly co-circular (↻,↻) or co-linear polarization with | or −, where the QD system can be reduced to a two- or three-level system, respectively, all four transitions are excited and the dynamics is governed by a mixture of the FSS-induced quantum beat and dephasing. One important control parameter is the polarization angle α of the exciting laser fields. In Fig. 3 the FWM signals as function of the time delay τ_{12} and the polarization angle (α, α) for a co-linear two pulse excitation are shown. The pulse area is $\theta_1 = \pi/5$. There is an excellent agreement between the measured signals in Fig. 3 (upper row) and the theoretical calculations in Fig. 3 (lower row).

As explained above, for $\alpha = 0°$ no FSS-induced beat is observed neither in the GXY nor the XYB signal, as the excitation is along the QD axis. Instead, we just observe a decay with the dephasing time T_2, which we here extract to $T_2 = 200$ ps. In contrast, for $\alpha = 45°$ the FSS-induced beat is maximal in the GXY signal. For this angle, an equal superposition of X and Y is excited invoking the FSS-induced quantum beat with a period of $T_\delta = 180$ ps. For intermediate angles between $\alpha = 0°$ and 45° there is a smooth transition with a less pronounced beating structure. Such angle dependent measurements can be used to determine the absolute axes (x, y) of the linearly polarized transitions GX and GY. In contrast

to the circularly polarized excitation, for linear excitation also the XB transitions is driven by the laser field and we see a finite XB signal. However, for such small pulse areas the XYB signal is very weak, because the biexciton transition is barely excited. Accordingly no quantum beats are seen in the XB signal. If the excitation were at higher pulse areas, also for the XYB signal we would obtain FSS-induced quantum beats.

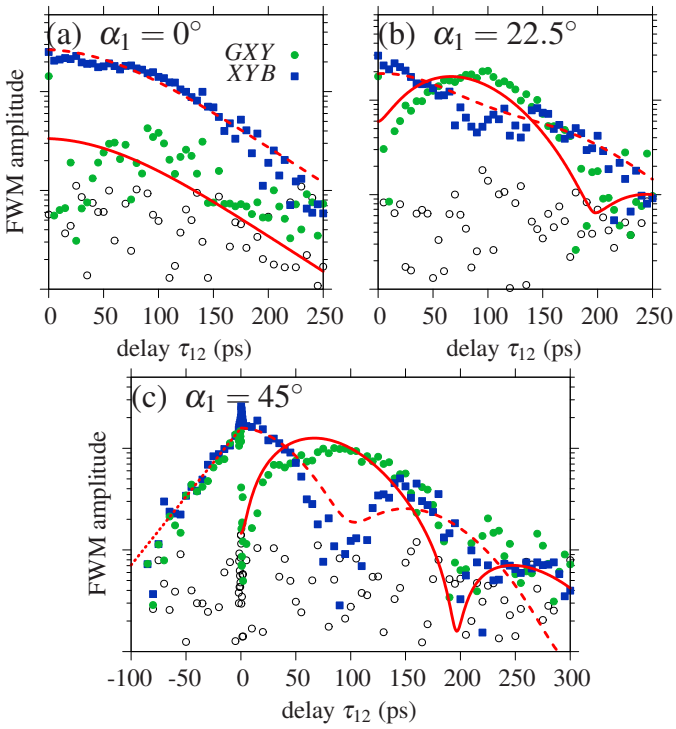

FIG. 4. **Coherence dynamics for cross-linear excitation.** Two-pulse FWM amplitude of the coherence dynamics of GXY and XYB transition for cross-polarized excitation with $\alpha_2 = \alpha_1 + 90°$ and (**a**) $\alpha_1 = 0°$, (**b**) $\alpha_1 = 22.5°$ and (**c**) $\alpha_1 = 45°$. Green dots and blue squares: experimental data of GXY and XYB, respectively. The background level is indicated by gray circles. Theoretical predictions are given by red lines.

We also analyze the angle dependence for cross-polarized driving in Fig. 4, where the angle of the second pulse is perpendicular to the first pulse, i.e., $\alpha_2 = \alpha_1 + 90°$. Here the pulse area is stronger with $\theta_1 = 3\pi/8$. For $\alpha_1 = 0°$ the FWM is primarily driven at XB via so-called Raman coherence induced between X and Y excitons in the second-order. Conversely, the GX almost vanishes, as shown in Fig. 4 a. Additionally, we see a bending of the curve for initial τ_{12}. This bending is attributed to inhomogeneous broadening caused by charge fluctuations in the QD environment, which we also account for in our model (see Methods section). For $\alpha = 45°$ shown in Fig. 4 c a pronounced oscillation is observed in both GXY and XYB. Having a closer look at small delays we find that the XYB signal starts with a maximum, while the GXY signal has a minimum attaining the noise level at $\tau_{12} = 0$. For the intermediate angle $\alpha = 22.5°$ the signals are almost equally strong and both exhibit pronounced FSS-induced beating. For $\alpha_1 = 45°$, we measured the FWM signal at negative delays τ_{12}, i.e., E_2 comes before E_1, presented in Fig. 4 c. Similar to the case of co-linear excitation with $\alpha = 0°$, E_2 excites a two-photon coherence between ground and biexciton state. The corresponding decay with the decoherence rate β_B is seen and can also be described by Eq. (3). For the decay rate β_B we find $T_B = 1/\beta_B = 91$ ps.

D. Population dynamics

Next, we focus on population dynamics. For a two-level system excited by three pulses, the first pulse creates a coherence, the second pulse creates a population and the third pulse induces the FWM signal which is probed. Therefore, information on the decay rate γ can be gained in such an experiment. In Fig. 5 a we show the GXY and XYB signal for the three pulse excitation with $\tau_{12} = 0.5$ ps as function of time delay τ_{23}. The analytical formula shows that both signals decay without any oscillation including an exponential decay with γ and 2γ. Instead of showing the general equation, we again evaluate the formulas for the explicit pulse area $\theta = 0.85\pi$ yielding

$$\mathcal{S}_{GXY} \propto e^{-\gamma\tau_{23}} - 0.29e^{-2\gamma\tau_{23}}, \tag{4a}$$
$$\mathcal{S}_{XYB} \propto e^{-\gamma\tau_{23}} + 0.76e^{-2\gamma\tau_{23}}. \tag{4b}$$

From the exponential decay of the FWM amplitude we retrieve a lifetime of $T_1 = 1/\gamma = 333$ ps.

When we choose a different excitation polarization, we find an oscillatory FWM signal in Fig. 5 b-d. Let us start with circularly polarized excitation ($\circlearrowleft, \circlearrowleft, \circlearrowleft$) shown in Fig. 5 b. The first two pulses create a population of the σ^+-exciton. From this state the third pulse cannot excite the biexciton. Consequently, at $\tau_{23} = 0$ the signal $\mathcal{S}_{XYB}$ is zero. Remember that σ^+ is a linear combination of the X and Y exciton. After the first two pulses, the populations and the polarization ρ_{XY} between X and Y contribute to the FWM. The latter oscillates with the FSS δ, which is directly reflected in the GXY signal. The period is $T_\delta = 196$ ps corresponding to a FSS $\delta = 21$ μeV. The quite different value in FSS compared to the QD used in Sec. II B shows that the FSS depends sensitively on the QD under examination. When the oscillation sets in, the exciton changes its character from σ^+ to σ^- due to the oscillating polarization ϱ_{XY}. When the system is in the σ^- exciton, the biexciton can be excited and the XYB signal has a maximum coinciding with GXY having a minimum. The equations for these dynamics are given

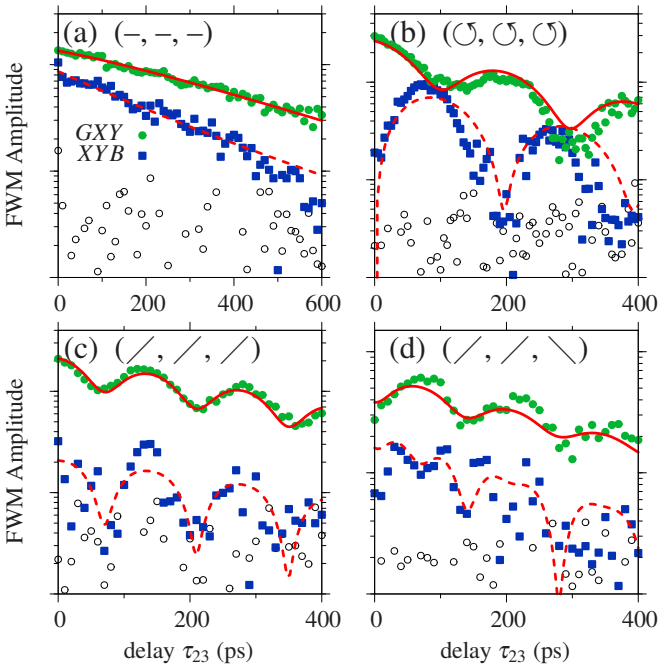

FIG. 5. **Population dynamics.** Three-pulse FWM amplitude displaying population dynamics of GXY and XYB for different polarization states of $E_{1,2,3}$ (**a**) $(-,-,-)$, (**b**) $(↺,↺,↺)$, (**c**) $(／,／,／)$ and (**d**) $(／,／,＼)$. Green dots and blue squares: experimental data of GXY and XYB, respectively; gray circles: indication of noise level; red lines: theoretical calculation.

by

$$\mathcal{S}_{G\sigma} = \mathcal{S}_{GXY} \tag{5a}$$
$$\propto \sqrt{6\cos\left(\frac{\delta\tau_{23}}{\hbar}\right) e^{-(\gamma+\beta_{XY})\tau_{23}} + 9e^{-2\gamma\tau_{23}} + e^{-2\beta_{XY}\tau_{23}}},$$
$$\mathcal{S}_{\sigma B} = \mathcal{S}_{XYB} \tag{5b}$$
$$\propto \sqrt{2\cos\left(\frac{\delta\tau_{23}}{\hbar}\right) e^{-(\gamma+\beta_{XY})\tau_{23}} - e^{-2\gamma\tau_{23}} - e^{-2\beta_{XY}\tau_{23}}}.$$

Similar to the coherence dynamics, the pulse area only determines the prefactor, but does not influence the time-dependence. We see an oscillatory term with the FSS δ, which is damped by the decay rate β_{XY} corresponding to the coherence ϱ_{XY} between the single excitons.

For linearly polarized excitation with a diagonal polarization $(／,／,／)$ presented in Fig. 5 c, again a superposition of X and Y with an oscillating polarization ϱ_{XY} is excited. Accordingly GXY oscillates likewise with the FSS. Note, that here a different QD was examined, for which we find the values $T_\delta = 140$ ps and $\delta = 30$ µeV. In contrast to the case of circular excitation, for linear excitation the biexciton can be directly addressed. Accordingly, the XYB signal starts with a maximum and then oscillates with the same period as the GXY signal. Finally, we examine the cross-polarized excitation with $(／,／,＼)$ in Fig. 5 d. A general trend is that GXY for cross-linear excitation oscillates opposite to the case of co-linear excitation. Because all polarizations contribute to the signal, also a mixture of the GX and GY occurs, leading to more complex behavior in the XYB signal involving higher harmonics of the beat frequency.

III. TRANSITIONS IN A CHARGE FLUCTUATING QD

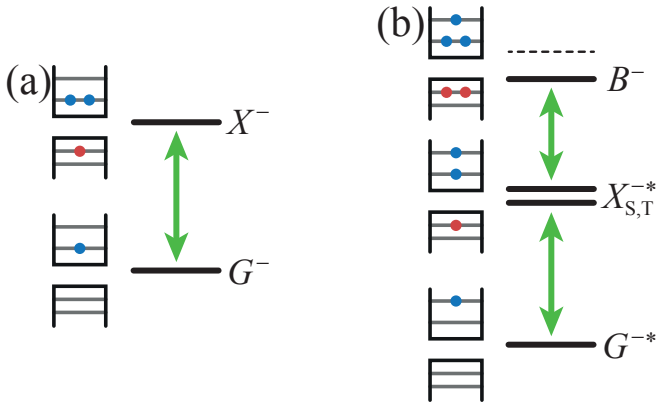

FIG. 6. **Charged exciton complexes.** Pictographic diagram of the (**a**) negative trion system and (**b**) the charged biexciton system with the excited trion states.

The charge state of a QD can fluctuate [32] over timescales several orders of magnitude faster than the integration time, which is in the 1-100 second range. Thus, not only the neutral exciton and biexciton appear in the FWM spectrum, but an assortment of different neutral and charged exciton transitions. One example of such a spectrum integrated over the delay time τ_{12} is shown in Fig. 7 a. The spectrum shows a variety of lines spread over a few meV. Because our sample is n-doped, we predominantly find dots which are initially charged with a single electron having the ground state G^-. When such a dot is excited the negatively charged exciton (trion) X^- is generated via the transition GX^- as depicted in Fig. 6 a. Due to the doping, GX^- has a high intensity and can be identified as the line at 1364.8 meV in Fig. 7a.

To identify the GX and XB transition of the neutral exciton, we look at the delay dependence of the coherence. The temporal behavior of all states is shown in Fig. 7 b, while the dynamics of the most fundamental lines, namely the GX, XB and GX^- line is displayed in more detail in Fig. 7 c. From the previous results, we know that the neutral GX and XB create a FWM signal for $\tau_{12} < 0$ via the two-photon coherence. In addition we checked that these transitions obey the corresponding polarization selection rules of GXYB (not shown), as detailed in the previous section II C. Thus we identify GX at 1367.5 meV and XB at 1364.5 meV. In contrast, negative trion lack FWM for $\tau_{12} < 0$, since the corresponding charged biexciton is spectrally too far to be excited [35].

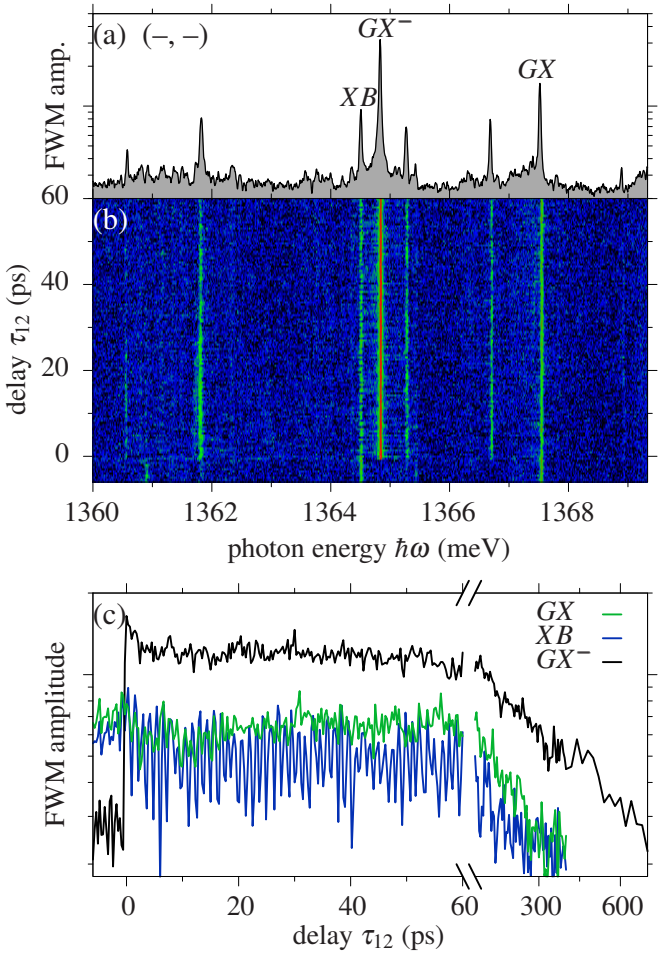

FIG. 7. **FWM of a charge fluctuating QD.** (**a**) Two-pulse FWM spectrum of a QD showing with (**b**) the corresponding dynamical behavior in τ_{12}. (**c**) FWM signal of the coherence dynamics for the GX, XB and GX^- transition.

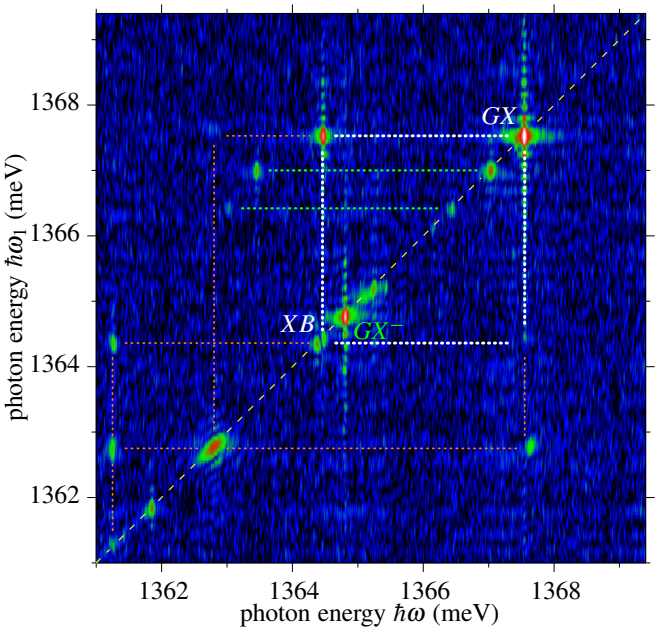

FIG. 8. **Two-dimensional four-wave-mixing.** 2D FWM spectroscopy map, revealing coherent couplings between exciton complexes generated by a charge fluctuating QD.

This is confirmed by looking at GX^- in Fig. 7 b and c, where GX^- is zero for $\tau_{12} < 0$. For positive time delays $\tau_{12} > 0$ we can discriminate between the transitions by the quantum beats. We see a strong quantum beat in the XB-transition induced by the BBE as in Fig. 2 e with a period $T_\Delta = 1.25$ ps. The BBE-induced oscillation survives on a long time scale of several hundreds of ps. The charged exciton transition GX^- does not show any dynamical behavior apart from a decay. This is expected, since G^- and X^- form a two-level system, depicted in Fig. 6 a, where only the dephasing alters the signal. We find a dephasing time of $T_2 = 270$ ps.

More information about the different exciton complexes can be gained from 2D spectral FWM maps. These maps are obtained by a 2D Fourier transform with respect to the real time t (horizontal axis) and the delay time τ_{12} between the pulses (vertical axis). While the transform with respect to t is assured by the spectrometer, the one with respect to τ_{12} requires adjusting the phase evolution for different delays [21] by implementing "the guiding star approach". As such a reference transition we choose the uncoupled GX^-. 2D FWM correlates resonances active in the first-order absorption, ω_1 (vertical axis), with the FWM ones, ω (horizontal axis). The spectrum can be regained from the 2D map by integrating over the y-axis. An advantage of the 2D spectrum is the possibility to detect couplings between different exciton transitions, which appear as off-diagonal peaks. The neutral exciton cast should be correlated among itself and strictly separated from charged configurations. An example of a 2D map from the same dot as in Fig. 7, but for a higher excitation power, is shown in Fig. 8. Let us focus on the neutral exciton complexes first: There are two points on the diagonal line at 1367.5 meV and at 1364.5 meV, which can be clearly identified as GX and XB transition, respectively. From the dynamics in Fig. 7 c, we have seen that XB shows a BBE-induced beating. In the 2D map, this is seen by a off-diagonal peak at (1364.5 meV, 1367.5 meV). We can identify a couple of other peaks, which are connected with the neutral exciton complex. These are marked by orange lines. These could stem from exciton or biexciton complexes, where an electron or a hole is in a p-shell, or from higher order non-linear processes [23].

For the charged excitons, we also see corresponding diagonal points. The strongest signal at 1364.8 meV belongs to the GX^- transition and is not connected to other transitions via off-diagonal peaks. This confirms, that $GX-$ does not couple to other transitions and G^- and X^- can be modeled as a two-level system. The coupling to the negatively charged biexciton B^- is unlikely. Remember that B^- consists of three electrons, two in the

s-shell and one in the p-shell, and two s-shell holes as depicted in Fig. 6 b. In principle, it is possible to have the transition from the trion X^- by exciting an exciton in the p-shell into the excited biexciton. However, the p-shell exciton is energetically far away, such that this transition is not covered by the laser pulse.

On the other hand, the charged biexciton B^- can decay by recombination of an s-shell exciton into the excited trion state $X^{-*}_{\mathrm{S,T}}$. In the excited trion state, one electron is in the s-shell and one in the p-shell. Due to the exchange interaction between the electrons the excited trion splits up into a singlet X^{-*}_{S} and a triplet X^{-*}_{T} state which are typically separated by a few meV [33, 34]. From the excited trion, again a recombination of an s-shell exciton can take place resulting in the excited charged ground state G^{-*}. Such a three-level system can give rise to off-diagonal peaks reflecting the coupling between the states. In the 2D map in Fig. 8 we see two such diagonal peaks at 1367 meV and 1366.5 meV. These have corresponding off-diagonals connected by green lines. It is highly likely that these are charged exciton complexes, because they are not connected to any neutral transition, and they can probably be identified with singlet-triplet transitions. However, because we cannot exclude that these peaks correspond to positively charged states, which would agree with recent photoluminescence excitation measurements [35], we refrain from a definite attribution. Complementary insights into the biexcitonic structure of charged states could be gained by inferring FWM beatings at negative delays.

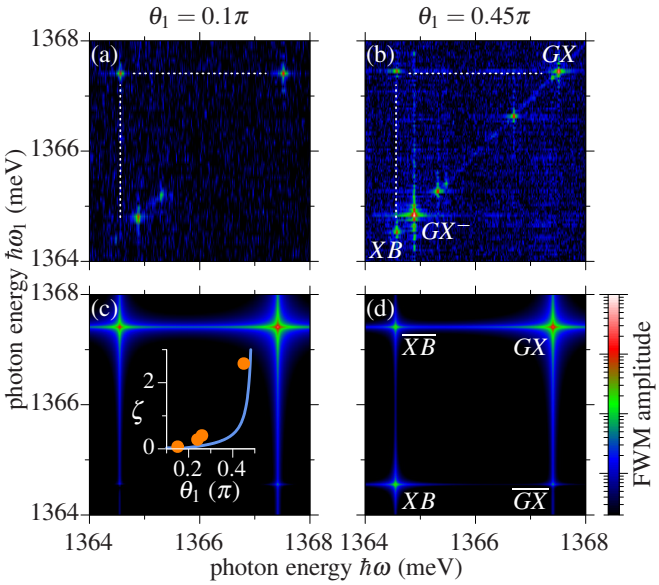

FIG. 9. **Pulse area dependence of 2D maps.** 2D FWM spectroscopy map of the exciton-biexciton system for an excitation with a pulse area of (**a, c**) $\theta_1 = 0.1\pi$ and (**b, d**) $\theta_1 = 0.45\pi$. Upper row: experimental data, lower row: theoretical calculations. The inset in (**c**) shows the strength of the ratio ζ of biexciton XB and correlation peak $\overline{XB}$ as function of pulse area θ_1; orange dots: experiment and blue curve: theory.

We complete the analysis of states by analyzing the dependence of the FWM maps on the pulse area. Higher-order FWM contributions, and hence the beating, are suppressed at lower excitation power. Accordingly the intensities of the peaks depend crucially on the excitation intensity. This is exemplified in Fig. 9, where the 2D map of the GXB system is shown for two different pulse areas of $\theta_1 = 0.1\pi$ and $\theta_1 = 0.45\pi$. The upper row shows the experimental data, while in the lower row theoretical predictions are plotted. For low pulse area $\theta_1 = 0.1\pi$, we clearly see the peak on the diagonal corresponding to GX. Also the off-diagonal peak is clearly visible, while the diagonal peak corresponding to XB vanishes. This is explained as follows: The coherence ϱ_{XB} is not excited for small pulse areas, however the second pulse E_2 (pulse area twice as large) probes both transitions and, thus, the interference peak is visible. For the pulse area $\theta_1 = 0.45\pi$, which is close to $\pi/2$, the off-diagonal peak is much weaker, while the diagonal peak for XB becomes visible. The inset in Fig. 9 shows the ratio of intensities $\zeta = I_{XB}/I_{\overline{XB}}$ between the diagonal XB peak and the off-diagonal $\overline{XB}$ peak (blue curve: theory; orange dots: experiment), which is increasing with increasing pulse area.

IV. CONCLUSION

In conclusion, we have presented a combined experimental and theoretical study on FWM signals retrieved from single, strongly-confined InAs QDs embedded in a low-Q semiconductor microcavity. The experimental results are in excellent agreement with simulations performed in a four-level system including FSS and BBE. The latter give rise to rich and pronounced quantum beats in the corresponding FWM signals, allowing to determine quantitative values. From all measurements population decay and dephasing rates were extracted. Additionally, we discussed the angle dependence of the FWM upon co- and cross-polarized excitation. We revealed and exploited coherences in a four-level system that are usually hidden, specifically as regards biexciton dephasing, studied via two-photon coherence, as well as the interplay between X and Y polarized excitons induced via Raman coherence. Using 2D FWM spectroscopy we confirmed the coupling between exciton and biexciton states and furthermore we identified charged exciton complexes. The FWM technique is a powerful tool to analyze coherent dynamics in few-level systems. Employing photonic structures enhancing optical coupling, it can directly be extended to other single photon emitters, like NV centers in diamond [36] or recently discovered single emitters in atomically thin semiconductors [37, 38], enabling to explore coherence, reveal couplings and implement quantum control protocols.

METHODS

Sample preparation and characterization

The MBE grown sample contains a layer of annealed and capped InAs QDs with a nominal density of 2.2×10^9 cm^{-2}. They are embedded in an asymmetric GaAs/AlGaAs micro-cavity exhibiting a low quality factor [16, 39–41] $Q = 170$, resulting in a mode centered at 910-915 nm with a FWHM of around 10 nm. The femtosecond laser pulse trains are spectrally matched with such a large spectral window and efficiently penetrate into the structure. Furthermore, the intra-cavity field is enhanced by a factor of $\sqrt{Q} = 13$ improving the coupling between $E_{1,2,3}$ and the electric dipole moment μ of the transition. Thus, the resonant field required to drive the FWM is reduced by a factor $Q^{3/2} \simeq 2200$ and the signal-to-noise ratio of the interferometrically detected FWM is amplified accordingly.

The sample is intentionally doped with Si (δ-doping with a nominal density of 1.8×10^{10} cm^{-2}; layer located 10 nm below the QD plane). To identify the spatial and spectral location of the QD transitions we perform hyperspectral imaging [21, 42]. In Fig. 10 a we present an example of such imaging performed in a confocal microphotoluminescence (PL) experiment. Each bright spot corresponds to a QD emission, primarily attributed to recombination of negative trions (GX^-) due to the n-doping. We detect high PL counting rates on the order of 10^5/sec at the QD saturation. Such an unusually bright PL emission is attributed to the presence of oval photonic defects on the sample surface [16, 41], acting as natural micro-lenses [18]. Additionally, the inhomogeneous broadening due to spectral wandering is largely reduced [16, 39] indicating an excellent structural quality of these QDs.

The FWM hyperspectral imaging at the same sample area and spectral range is shown in Fig. 10 b. The three QDs at $(x, y) \approx (-2\ \mu\text{m}, -5\ \mu\text{m})$, $(2\ \mu\text{m}, -5\ \mu\text{m})$ and $(7\ \mu\text{m}, -4\ \mu\text{m})$ (marked with green boxes in Fig. 10) exhibit both PL and FWM signals and were used to align the figures. However, other QDs show different distribution of the peak heights in FWM as compared to the PL. This is expected from the different properties determining the signal strength in both measurements: in FWM the dipole moment is probed, while in PL generally the more complex phonon-assisted carrier relaxation combined with a capture of the exciton also lead to a signal. To demonstrate the high spectral and spatial selectivity of the FWM compared to the PL, Figs. 10 c and d compare both PL and FWM obtained from the same sample spot, defined by the diffraction limited size (0.7 µm) of the excitation laser. In Fig. 10 c we show a neutral exciton complex, which is only present in few % of the QDs. The exciton-biexciton system is straightforwardly recognized in FWM, but it is difficult to be identified in PL, because of a lacking XB emission line. Figure 10 d shows the PL and FWM spectra of the fundamental trion line corresponding to a negatively charged QD. A zoom-in of the spatial shape of the XB and GX transition is shown in Fig. 10 e and f, respectively.

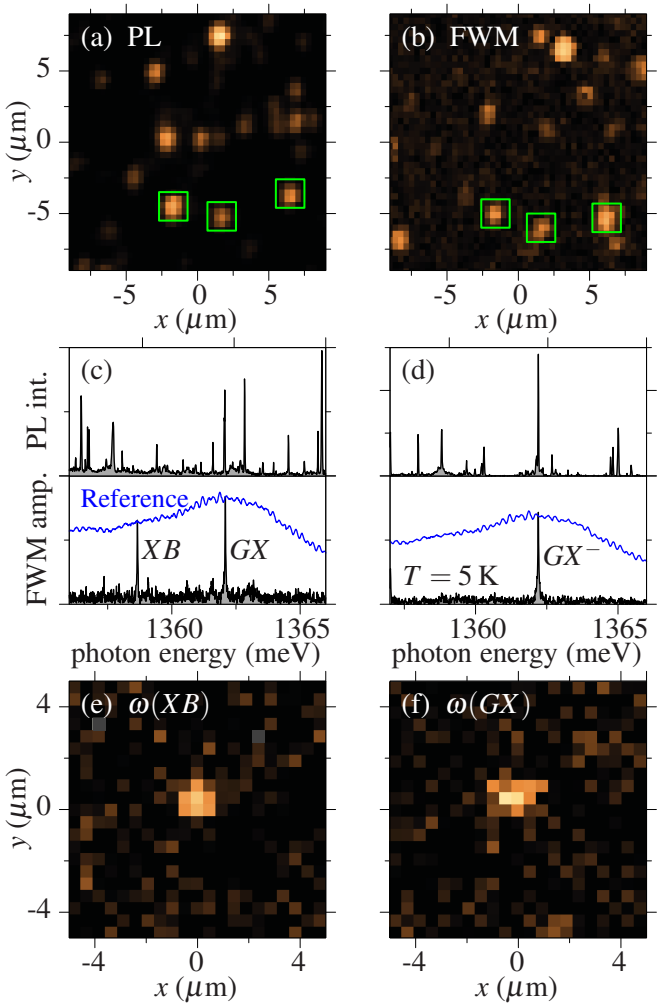

FIG. 10. **Sample characterization.** Hyperspectral image of the sample for (**a**) PL and (**b**) FWM measurements. (**c,d**) PL and FWM spectra of a single QD. Blue indicates the spectrum of the laser pulse as reference. (**e,f**) Hyperspectral FWM image of of XB and GX transition.

Theoretical Model

The Hamiltonian for circularly polarized excitation (cf. Fig. 1 a) reads

$$H = \sum_{\nu} \hbar\omega_\nu \left|\nu\right\rangle \left\langle\nu\right| - \sum_{\nu,\nu'} \hbar M_{\nu\nu'} \left|\nu\right\rangle \left\langle\nu'\right| + H_{\text{exc}} \quad (6)$$

with the basis states

$$\left|\nu\right\rangle \in \{\left|G\right\rangle, \left|\sigma^-\right\rangle, \left|\sigma^+\right\rangle, \left|B\right\rangle\} \ . \quad (7)$$

Correspondingly the energies are $\hbar\omega_G = 0$, $\hbar\omega_{\sigma^-} = \hbar\omega_{\sigma^+} = \hbar\omega_\sigma$ and $\hbar\omega_B = 2\hbar\omega_\sigma - \Delta$, where Δ is the BBE.

Due to the Coulomb exchange interaction the two single exciton levels interact via

$$H_{\text{exc}} = \frac{\delta}{2}\left(\left|\sigma^-\right\rangle\left\langle\sigma^+\right| + \left|\sigma^+\right\rangle\left\langle\sigma^-\right|\right) \tag{8}$$

The light field coupling

$$\underline{M} = \begin{pmatrix} 0 & \Omega^*_{\sigma^+} & \Omega^*_{\sigma^-} & 0 \\ \Omega_{\sigma^+} & 0 & 0 & \Omega^*_{\sigma^-} \\ \Omega_{\sigma^-} & 0 & 0 & \Omega^*_{\sigma^+} \\ 0 & \Omega_{\sigma^-} & \Omega_{\sigma^+} & 0 \end{pmatrix} \tag{9}$$

describes the allowed transitions via the Rabi frequencies

$$\Omega_{\sigma^\pm} = \sum_j \frac{M_0}{\hbar}\mathbf{E}_j \cdot \mathbf{e}^*_{\sigma^\pm}. \tag{10}$$

M_0 is the bulk dipole matrix element and $\mathbf{e}_{\sigma^\pm}$ the polarization vector. The polarization of the system is given by

$$\begin{aligned}\mathbf{p} = \quad & M_0\left(|0\rangle\left\langle\sigma^+\right| + \left|\sigma^-\right\rangle\langle B|\right)\mathbf{e}_{\sigma^+} \\ & + M_0\left(|0\rangle\left\langle\sigma^-\right| + \left|\sigma^+\right\rangle\langle B|\right)\mathbf{e}_{\sigma^-}.\end{aligned}$$

This Hamiltonian can be transformed into the basis for linearly polarized excitons (cf. Fig. 1 b), which are the eigenstates of $\sum_\nu \hbar\omega_\nu |\nu\rangle\langle\nu| + H_{\text{exc}}$. The transformation is calculated by

$$|X\rangle = \frac{1}{\sqrt{2}}\left(|\sigma^+\rangle + |\sigma^-\rangle\right), \tag{11}$$

$$|Y\rangle = \frac{i}{\sqrt{2}}\left(|\sigma^+\rangle - |\sigma^-\rangle\right). \tag{12}$$

By the diagonalization the degeneracy of the single excitons is lifted and the exciton energies are $\hbar\omega_X = \hbar\omega_\sigma - \delta/2$ and $\hbar\omega_Y = \hbar\omega_\sigma + \delta/2$. The light field coupling changes to

$$\underline{M} = \begin{pmatrix} 0 & \Omega^*_X & \Omega^*_Y & 0 \\ \Omega_X & 0 & 0 & \Omega^*_X \\ \Omega_Y & 0 & 0 & \Omega^*_Y \\ 0 & \Omega_X & \Omega_Y & 0 \end{pmatrix} \tag{13}$$

with

$$\Omega_X = \frac{1}{\sqrt{2}}\left(\Omega_{\sigma^+} + \Omega_{\sigma^-}\right), \quad \Omega_Y = \frac{i}{\sqrt{2}}\left(\Omega_{\sigma^+} - \Omega_{\sigma^-}\right).$$

The time evolution of the density matrix ϱ is calculated assuming a sum of δ-pulses yielding the Rabi frequencies for circular polarization

$$\Omega_{\sigma^\pm} = \sum_j \frac{\theta_j^{\sigma^\pm}}{2} e^{i\varphi_j^{\sigma^\pm}} \delta(t - t_j) \tag{14}$$

with arrival times t_j, pulse areas $\theta_j^{\sigma^\pm}$ and phases $\varphi_j^{\sigma^\pm}$. For a pulse sequence with linear polarizations α_j with respect to X and pulse areas θ_j the Rabi frequencies read

$$\begin{aligned}\Omega_X &= \sum_j \sqrt{2}\,\theta_j e^{i\phi_j}\cos(\alpha_j), \\ \Omega_Y &= \sum_j -\sqrt{2}\,\theta_j e^{i\phi_j}\sin(\alpha_j).\end{aligned}$$

In the case of δ-pulses the time evolution of the system can be calculated by matrix multiplication [19]. In between the pulses the dynamics is given by

$$\rho_{\nu\nu'}(t) = \rho_{\nu\nu'}(0)e^{i\Lambda_{\nu\nu'}(t)} \tag{15}$$

with

$$\begin{aligned}\Lambda_{\nu\nu'} &= \omega_\nu - \omega_{\nu'} + i\beta_{\nu\nu'}, \\ \underline{\beta} &= \begin{pmatrix} 0 & \beta & \beta & \beta_B \\ \beta & 0 & \beta_{XY} & \beta \\ \beta & \beta_{XY} & 0 & \beta \\ \beta_B & \beta & \beta & 0 \end{pmatrix}.\end{aligned}$$

β, β_B and β_{XY} are the dephasing rates described in Sec. IV. The decay of the exciton and biexciton is modeled by a single decay rate γ, which leads to the following equations of motion for the diagonal elements of the density matrix:

$$\begin{aligned}\varrho_{BB}(t) &= \varrho_{BB}(0)e^{-2\gamma t} \\ \varrho_{XX}(t) &= [\varrho_{XX}(0) + \varrho_{BB}(0)(1 - e^{-\gamma t})]e^{-\gamma t} \\ \varrho_{YY}(t) &= [\varrho_{YY}(0) + \varrho_{BB}(0)(1 - e^{-\gamma t})]e^{-\gamma t} \\ \varrho_{GG}(t) &= 1 - [\varrho_{XX}(0) + \varrho_{YY}(0) + \varrho_{BB}(0)(2 - e^{-\gamma t})]e^{-\gamma t}\end{aligned}$$

The time $t = 0$ corresponds to the time directly after each pulse.

From this, we can calculate the dynamics of all elements of the density matrix, in other words, of all populations and coherences. The FWM signal is theoretically extracted by analyzing the phase dependence of the polarization. In general, all polarizations have parts depending on different orders and combinations of the phases φ_i of the pulses. The two-pulse FWM for coherence dynamics is given by the phase combination $(2\varphi_2 - \varphi_1)$, while the three-pulse FWM for the population dynamics is characterized by the phase combination $(\varphi_3 + \varphi_2 - \varphi_1)$ which model the heterodyning at $(2\Omega_2 - \Omega_1)$ and $(\Omega_3 + \Omega_2 - \Omega_1)$. This identifies the polarization of the FWM signal indicated by p^{FWM}. For the sake of simplicity, in the case of population dynamics we use $\tau_{12} = 0$ ps to mimic the short time delay between the first two pulses. From the polarization the FWM signal $\mathcal{S}_{\nu\nu'}$ is obtained by a Fourier transform at the selected frequency

$$\mathcal{S}_{\nu\nu'} = \left|\int_0^\infty p^{\text{FWM}}\, e^{i\omega t}\,\mathrm{d}t\right|_{\omega=\omega_\nu-\omega_{\nu'}}. \tag{16}$$

If the polarization α is not along one axis of the QD, the signals are added according to the angle of the heterodyning (reference) beam α_r with $\mathcal{S}_{GXY} = \cos^2(\alpha_r)\mathcal{S}_{GX} + \sin^2(\alpha_r)\mathcal{S}_{GY}$.

In the FWM signal, charge fluctuations can play an important role leading to an inhomogeneous broadening via spectral wandering of individual transitions. This phenomenon induces a photon echo in FWM transients of single QDs, when probing the coherence [17, 28, 30].

The residual inhomogeneous broadening (i.e. up to several homogeneous linewidths) can be included in the calculations by multiplying the FWM-polarization with a Gaussian function [30] as follows:

$$p^{\mathrm{FWM}} \rightarrow p^{\mathrm{FWM}}\, e^{-\frac{(t-\tau_{12})^2}{2\sigma^2}} \tag{17}$$

For most cases the inhomogeneous broadening can be neglected. We only included it to model the data in Fig. 4 with $\sigma = 67$ ps, which corresponds to an energetic broadening of $\hbar\sigma \approx 10$ µeV.

[1] N. H. Bonadeo, J. Erland, D. Gammon, D. Park, D. S. Katzer, and D. G. Steel, Science **282**, 1473 (1998).
[2] P. Michler, *Single quantum dots: Fundamentals, applications and new concepts* (Springer, Berlin, 2003).
[3] A. J. Ramsay, Semicond. Sci. Technol. **25**, 103001 (2010).
[4] L. Monniello, C. Tonin, R. Hostein, A. Lemaitre, A. Martinez, V. Voliotis, and R. Grousson, Phys. Rev. Lett. **111**, 026403 (2013).
[5] I. A. Akimov, J. T. Andrews, and F. Henneberger, Phys. Rev. Lett. **96**, 067401 (2006).
[6] G. Bacher, R. Weigand, J. Seufert, V. D. Kulakovskii, N. A. Gippius, A. Forchel, K. Leonardi, and D. Hommel, Phys. Rev. Lett. **83**, 4417 (1999).
[7] R. Seguin, A. Schliwa, S. Rodt, K. Pötschke, U. W. Pohl, and D. Bimberg, Phys. Rev. Lett. **95**, 257402 (2005).
[8] R. J. Young, R. M. Stevenson, A. J. Shields, P. Atkinson, K. Cooper, D. A. Ritchie, K. M. Groom, A. I. Tartakovskii, and M. S. Skolnick, Phys. Rev. B **72**, 113305 (2005).
[9] R. M. Stevenson, R. J. Young, P. Atkinson, K. Cooper, D. A. Ritchie, and A. J. Shields, Nature **439**, 179 (2006).
[10] N. Akopian, N. H. Lindner, E. Poem, Y. Berlatzky, J. Avron, D. Gershoni, B. D. Gerardot, and P. M. Petroff, Phys. Rev. Lett. **96**, 130501 (2006).
[11] F. Ding, R. Singh, J. D. Plumhof, T. Zander, V. Křápek, Y. H. Chen, M. Benyoucef, V. Zwiller, K. Dörr, G. Bester, G. Bester, A. Rastelli, and O. G. Schmidt, Phys. Rev. Lett. **104**, 067405 (2010).
[12] C. Tonin, R. Hostein, V. Voliotis, R. Grousson, A. Lemaitre, and A. Martinez, Phys. Rev. B **85**, 155303 (2012).
[13] W. Langbein and B. Patton, Opt. Lett. **31**, 1151 (2006).
[14] T. Voss, I. Rückmann, J. Gutowski, V. M. Axt, and T. Kuhn, Phys. Rev. B **73**, 115311 (2006).
[15] G. Moody, R. Singh, H. Li, I. A. Akimov, M. Bayer, D. Reuter, A. D. Wieck, and S. T. Cundiff, Phys. Rev. B **87**, 045313 (2013).
[16] F. Fras, Q. Mermillod, G. Nogues, C. Hoarau, C. Schneider, M. Kamp, S. Höfling, W. Langbein, and J. Kasprzak, Nature Photon. **10**, 155-158 (2016).
[17] Q. Mermillod, T. Jakubczyk, V. Delmonte, A. Delga, E. Peinke, J.-M. Gérard, J. Claudon, and J. Kasprzak, accepted in Phys. Rev. Lett. (2016).
[18] M. Gschrey, A. Thoma, P. Schnauber, M. Seifried, R. Schmidt, B. Wohlfeil, L. Krüger, J.-H. Schulze, T. Heindel, S. Burger, A. Strittmatter, S. Rodt, and S. Reitzenstein, Nature Comm. **6** (2015).
[19] A. Vagov, V. M. Axt, and T. Kuhn, Phys. Rev. B **66**, 165312 (2002).
[20] V. M. Axt, T. Kuhn, A. Vagov, and F. M. Peeters, Phys. Rev. B **72**, 125309 (2005).
[21] J. Kasprzak, B. Patton, V. Savona, and W. Langbein, Nature Photon. **5**, 57 (2011).
[22] S. T. Cundiff, J. Opt. Soc. Am. B **29**, A69 (2012).
[23] X. Dai, M. Richter, H. Li, A. D. Bristow, C. Falvo, S. Mukamel, and S. T. Cundiff, Phys. Rev. Lett. **108**, 193201 (2012).
[24] W. Langbein, Rivista del nuovo cimento **33**, 255 (2010).
[25] B. Patton, U. Woggon, and W. Langbein, Phys. Rev. Lett. **95**, 266401 (2005).
[26] D. E. Reiter, T. Kuhn, M. Glässl, and V. M. Axt, J. Phys. Condens. Matter **26**, 423203 (2014).
[27] W. Langbein, P. Borri, U. Woggon, V. Stavarache, D. Reuter, and A. D. Wieck, Phys. Rev. B **69**, 161301 (2004).
[28] B. Patton, W. Langbein, U. Woggon, L. Maingault, and H. Mariette, Phys. Rev. B **73**, 235354 (2006).
[29] J. Kasprzak and W. Langbein, Phys. Rev. B **78**, 041103 (2008).
[30] J. Kasprzak, S. Portolan, A. Rastelli, L. Wang, J. D. Plumhof, O. G. Schmidt, and W. Langbein, New J. Phys. **15**, 055006 (2013).
[31] A. Krügel, A. Vagov, V. M. Axt, and T. Kuhn, Phys. Rev. B **76**, 195302 (2007).
[32] A. V. Kuhlmann, J. Houel, A. Ludwig, L. Greuter, D. Reuter, A. D. Wieck, M. Poggio, and R. Warburton, Nature Phys. **9**, 570 (2013).
[33] B. Urbaszek, R. J. Warburton, K. Karrai, B. D. Gerardot, P. M. Petroff, and J. M. Garcia, Phys. Rev. Lett. **90**, 247403 (2003).
[34] I. A. Akimov, K. V. Kavokin, A. Hundt, and F. Henneberger, Phys. Rev. B **71**, 075326 (2005).
[35] Y. Kodriano, E. R. Schmidgall, Y. Benny, and D. Gershoni, Semicond. Sci. Technol. **29**, 053001 (2014).
[36] I. Aharonovich, S. Castelletto, D. A. Simpson, C. H. Su, A. D. Greentree, and S. Prawer, Rep. Prog. Phys. **74**, 076501 (2011).
[37] P. Tonndorf, R. Schmidt, R. Schneider, J. Kern, M. Buscema, G. A. Steele, A. Castellanos-Gomez, H. S. J. van der Zant, S. Michaelis de Vasconcellos, and R. Bratschitsch, Optica **2**, 347 (2015).
[38] M. Koperski, K. Nogajewski, A. Arora, V. Cherkez, P. Mallet, J.-Y. Veuillen, J. Marcus, P. Kossacki, and M. Potemski, Nature Nanotech. **10**, 503.
[39] Y.-M. He, Y. He, Y.-J. Wei, D. Wu, M. Atatüre, C. Schneider, S. Höfling, M. Kamp, C.-Y. Lu, and J.-W. Pan, Nature Nanotech. **8**, 213 (2013).
[40] Y. He, Y.-M. He, Y.-J. Wei, X. Jiang, M.-C. Chen, F.-L. Xiong, Y. Zhao, C. Schneider, M. Kamp, S. Höfling, C.-Y. Lu, and J.-W. Pan, Phys. Rev. Lett. **111**, 237403

(2013).
[41] S. Maier, P. Gold, A. Forchel, N. Gregersen, J. Mørk, S. Höfling, C. Schneider, and M. Kamp, Optics Express **22**, 8136 (2014).
[42] J. Kasprzak and W. Langbein, Phys. Status Solidi B **246**, 820 (2009).

ACKNOWLEDGEMENTS

We acknowledge the support by the ERC Starting Grant PICSEN, contract no. 306387. D.E.R. is grateful for financial support from the DAAD within the P.R.I.M.E. program.

Author contributions: Q.M., V.D. and J.K. performed measurements. D.W. did the theoretical modeling. C.S, M.K. and S.H. fabricated the sample. W.L. and G.N. provided technical assistance. Q.M., D.W. D.E.R, T.K. and J.K. prepared the figures and wrote the paper.